Chinese Journal of Mechanical Engineering

ORIGINAL ARTICLE

Open Access

Failure Analysis of Dissimilar Metal Welds between Ferritic Heat Resistant Steels and Austenitic Stainless Steels in Power Plant

Xiaogang Li[1*], Junfeng Nie[1*], Xin Wang[1], Kejian Li[2] and Haiquan Zhang[1]

Abstract

This study analysed the failure of dissimilar metal welds (DMWs) between ferritic heat resistant steels and austenitic stainless steels and investigated its influencing factors by means of numerical simulation, microstructure characterization and mechanical property test. Under the long-term high-temperature service condition in practical power plant, the DMW failure mode was along the interface between nickel-based weld metal (WM) and ferritic heat resistant steel, and the failure mechanism was stress/strain concentration, microstructure degradation and oxidation coupling acting on the interface. The numerical simulation results show that interface stress/strain concentration was due to the differences in coefficient of thermal expansion and creep strength, and the degree of stress/strain concentration was related to service time. The ferrite band formed at the WM/ferritic steel interface was prone to cracking, attracting the fracture along the interface. The interface crack allowed oxidation to develop along the WM/ferritic steel interface. During long-term service, the interface stress/strain concentration, microstructure and oxidation all evolved, which synergistically promoted interface failure of DMW. However, only under the long-term service of low stress conditions could trigger the interface failure of DMW. Meanwhile, long-term service would reduce the mechanical strength and plasticity of DMW.

Keywords Dissimilar metal weld, Failure, Interface, Stress/strain concentration, Microstructure, Oxidation

1 Introduction

Ferritic heat resistant steels and austenitic stainless steels have been widely employed in coal-fired/nuclear power plants [1–3]. Among them, austenitic stainless steels are usually used in higher temperature positions of the unit due to their high creep rupture strength and outstanding oxidation resistance, and ferritic heat resistant steels are usually used in lower temperature positions of the unit, which could achieve flexible material selection and cost savings. Ferritic heat resistant steels in power plants are mainly bainitic steel containing ~ 2%Cr (commonly known as low-alloy steel) and martensitic steel containing ~ 9%Cr (commonly known as 9Cr steel) [1, 2, 4]. Welding is applied to the connection of ferritic heat resistant steels and austenitic stainless steels [5]. Thus, there are thousands of dissimilar metal welds (DMWs) between ferritic heat resistant steels and austenitic stainless steels in one unit of power plant [2, 5]. In order to fabricate the above DMWs, early austenitic stainless steel filler metal was used as filler material [6]. However, engineering practice experience shows that premature failure of DMW always occurred along the interface between austenitic weld metal (WM) and ferritic steel [7], and thus the service life of DMW was decreased and cannot

*Correspondence:
Xiaogang Li
xiaogangli@mail.tsinghua.edu.cn
Junfeng Nie
niejf@tsinghua.edu.cn
[1] Institute of Nuclear and New Energy Technology, Key Laboratory of Advanced Reactor Engineering and Safety of Ministry of Education, Tsinghua University, Beijing 100084, China
[2] Department of Mechanical Engineering, Tsinghua University, Beijing 100084, China

be predicted. The premature failure of the DMW filled with austenitic stainless steel filler metal was related to the obvious thermal stress at the WM/ferritic steel interface and serious carbon migration across the WM/ferritic steel interface during long-term high-temperature service [7]. The obvious thermal stress at the austenitic WM/ferritic steel interface was caused by the huge difference in coefficient of thermal expansion (CTE) between the austenitic material and ferritic material, and the serious carbon migration across the interface was caused by the huge difference of carbon chemical potential on both sides of the interface [2, 8]. In order to avoid DMW premature failure, nickel-based filler metal has been used to replace austenitic stainless steel filler metal. Because of the reduction in the CTE and carbon chemical potential on both sides of the WM/ferritic steel interface, the thermal stress at the nickel-based WM/ferritic steel interface and the carbon migration across the nickel-based WM/ferritic steel interface were weakened during service. As a result, the service performance of the DMW with nickel-based WM was improved over that of the DMW with austenitic WM [1, 9, 10]. However, the premature failure of the DMW cannot be completely avoided because stress concentration and carbon migration behaviors still persist at the nickel-based WM/ferritic steel interface. Consequentially, the failure analysis during service is a prerequisite for the improvement of service performance of DMWs.

For the DMW with nickel-based WM, the failure always occurred in the ferritic steel side of it. There are three failure modes: a) nickel-based WM/ferritic steel interface failure [2, 11–16]; b) ferritic heat affected zone (HAZ) failure [11–13, 17–21]; c) ferritic base metal (BM) failure [17, 18, 22]. Different failure modes correspond to different failure mechanisms. The ferritic BM failure mode was usually plastic cracking induced by the growth of dimples [17, 18]. The ferritic HAZ failure mode was the result of Type IV crack [19], which was caused by matrix softening, precipitate coarsening, and lacking sufficient precipitates pinning at the grain boundaries [19–21, 23–25]. Especially, the interface failure mode would lead to the most significant loss of DMW service life [26]. The previous literature suggested that the interface failure was mainly controlled by stress and strain concentrations [13, 27, 28], oxide notch [14, 16], and microstructure degradation [12, 15, 29, 30]. In Refs. [13, 27, 28], the stress and strain analyses were conducted under DMW creep tests, in which the load was larger than that under service conditions in a practical power plant. Matsunaga et al. [14] believed that the interface oxide notch in the ferritic steel side was the main reason for the DMW failure, but they did not show sufficient results on the influences of stress and strain on the failure. The classical work shows that the microstructure evolution near the WM/ferritic steel interface had an important influence on DMW failure. Carbon migration across the nickel-based WM/ferritic steel interface led to the formation of type I carbides along the interface, aggravating the uncoordinated deformation at the interface and forming stress concentration at the interface, resulting in the initiation of creep voids along the interface and the interface failure of the DMW [11]. However, Parker et al. [31] conducted creep tests of the DMW with type I carbide and the DMW without type I carbide under the same conditions, and they found that when the applied stress was 40 MPa ~ 50 MPa, both DMWs ruptured along the nickel-based WM/ferritic steel interface and the life was similar, which meant that the formation of type I carbides was not the most fundamental reason leading to DMW premature failure. In summary, the DMW failure mechanism is complicated and failure analysis should be carried out further. On the one hand, most of the researches on the failure analysis of DMW were carried out under the creep condition in the laboratory, in which the applied stress was usually higher than the actual service stress, so these results cannot be directly applied to the failure analysis of DMW in practical power plants. Zhang et al. [26] pointed out that stress level determined the failure mechanism. On the other hand, the DMW failure research comprehensively considering mechanics factor, microstructure factor and oxidation factor is limitedly reported. Therefore, it is necessary to conduct an analysis of the failure behaviors of DMWs under practical service conditions in power plants while comprehensively considering the interface microstructure, stress and strain concentrations and interface oxidation.

In this study, we conducted failure analysis for the low-alloy steel/austenitic stainless steel DMW filled with nickel-based metal and the 9Cr steel/austenitic stainless steel DMW filled with nickel-based metal from practical power plants, by the combination of experiment and simulation methods. Firstly, finite element analysis (FEA) method was used to investigate the stress and strain concentrations in the DMWs during service, and we quantitatively analyzed the stress and strain evolution during long-term service. Furthermore, the interfacial microstructure, chemical composition and interface oxidation of two types of ex-service DMWs were characterized, and we analysed the effects of microstructure and oxidation on the DMW failure. In addition, high-temperature tensile tests were performed for the DMWs before and after service, to clarify influence of long-term exposure on mechanical properties of DMWs. Finally, failure mechanisms and behaviors of DMWs during the long-term service in practical power plants were discussed.

2 Materials and Experiments

2.1 Materials and DMW Fabrication

In this study, the main materials were ferritic heat resistant steels, which were connected with austenitic stainless steel to fabricate DMWs. There were two types of ferritic heat resistant steels used: i) 9Cr steel; ii) low-alloy steel. The chemical composition (wt. %) of 9Cr steel is 9.0 Cr, 0.1 C, 0.4 Mn, 1.0 Mo, 0.2 V, 0.3 Si, 0.3 Ni, 0.08 Nb and Fe balanced. The chemical composition (wt. %) of low-alloy steel is 1.9 Cr, 0.6 Mo, 0.1 C, 0.5 Si, 0.6 Mn, 0.4 W, 0.4 V and Fe balanced. The chemical composition (wt. %) of austenitic stainless steel is 18.4 Cr, 11.3 Ni, 0.07 C, 0.8 Nb, 0.6 Si, 1.5 Mn and Fe balanced. To fabricate DMWs between ferritic heat resistant steels and austenitic stainless steels, tungsten inert gas (TIG) welding was employed. The filler material was Inconel 82 wire (ERNiCr-3). The chemical composition (wt. %) of ERNiCr-3 is 20.0 Cr, 0.1 C, 3.0 Fe, 3.0 Mn, 2.0 Nb, $\leq$ 0.75 Ti, $\leq$ 0.5 Cu, $\leq$ 0.12 Co, 0.5 Si and Ni balance. Groove angle of 60° and multi-layer technology were applied for TIG welding. TIG was performed under a welding current of ~ 120 A and an arc voltage of ~ 10 V. Pure argon was used as the shielding gas, with a flow rate of ~ 10 L/min.

2.2 Service Condition of the DMWs

The DMWs were located in steam tubes in power plants. The tube containing low-alloy steel DMW served at a steam temperature of 541 °C and steam pressure of 17.5 MPa for 15000 h. The tube containing low-alloy steel DMW had been operated in the superheater of the 320 MW subcritical unit in the power plant in China. The tube containing 9Cr steel DMW served at a steam temperature of 541 °C and steam pressure of 3.5 MPa for 67000 h, which was in the reheater of the 300 MW subcritical unit in the power plant of China. Another tube containing 9Cr steel DMW served at steam temperature of 570 °C and steam pressure of 25 MPa for 80000 h, which was in the superheater in the power plant in China. After long-term service, the DMWs were taken from the ex-service steam tubes and were analyzed.

2.3 Performance and Characterization Tests

The high-temperature tensile tests were conducted for the DMWs before and after service. The tensile specimens were machined from the steam tubes. The tensile load direction was perpendicular to the welding direction. The tensile specimen contained WM, HAZ and BMs. The tensile specimens were loaded at 600 ℃, until they were completely broken. After tensile tests, the failure path was observed by optical microscopy (OM), and the fracture appearance of the broken specimen was observed by scanning electron microscopy (SEM). In addition, the interface between nickel-based WM and ferritic heat resistant steel HAZ was observed by SEM, and its chemical composition was analysed by electron probe microanalysis (EPMA). The specimen for microstructure observation was ground to 5000 grit, mechanically polished and chemically etched. For the DMW involving low-alloy steel, the etched solution of nitric acid (3 vol.%) and ethyl alcohol (97 vol.%) was used. For the DMW involving 9Cr steel, Villela' s reagent (100 mL ethanol + 5 mL HCl + 1 g picric acid) was used as the etched solution. Furthermore, electron backscatter diffraction (ESBD) was carried out for the ex-service DMW specimen to investigate damage. The specimens for EPMA and EBSD were mechanically polished and then ion beam polished with an ion beam milling system.

3 Results and Discussion

Failure mechanism determines the service life of DMWs containing ferritic heat resistant steels, which is related to three factors, namely, mechanical state, microstructure and oxidation. The related research under actual service conditions was limited. In this study, we investigated the DMWs in steam tubes in power plants, and the failure was analyzed. Especially, the effects of mechanics factor, microstructure factor and oxidation factor on failure and were considered separately, the correlation between service condition and failure mechanism was clarified.

3.1 Failure of Steam Tubes Containing DMWs between Ferritic Heat Resistant Steel and Austenitic Stainless Steel

We obtained the low-alloy steel DMW located in the ex-service steam tube and the 9Cr steel DMW located in the ex-service steam tube. The outer diameter and wall thickness of the steam tube containing low-alloy steel DMW were 53 mm and 8 mm, and the low-alloy steel DMW had been operated at 541 ℃ for 15000 h. The outer diameter and wall thickness of the steam tube containing 9Cr steel DMW were 63 mm and 4 mm, and the 9Cr steel DMW had been operated at 541 ℃ for 67000 h. Figure 1 shows the cross-sectional images of the ferritic heat resistant steel side of the DMWs after long-term service. The surfaces of steam tube had been oxidized. It is worth noting that the low-alloy steel DMW ruptured, and failure path was along the interface between nickel-based WM and low-alloy steel. The contribution of stress and strain concentrations during service to failure was difficult to obtain experimentally. Thus, the ex-service steam tube containing low-alloy steel DMW and the ex-service steam tube containing 9Cr steel DMW were modeled in ABAQUS, and FEA on stress and strain evolution was conducted. The influences of mechanical state

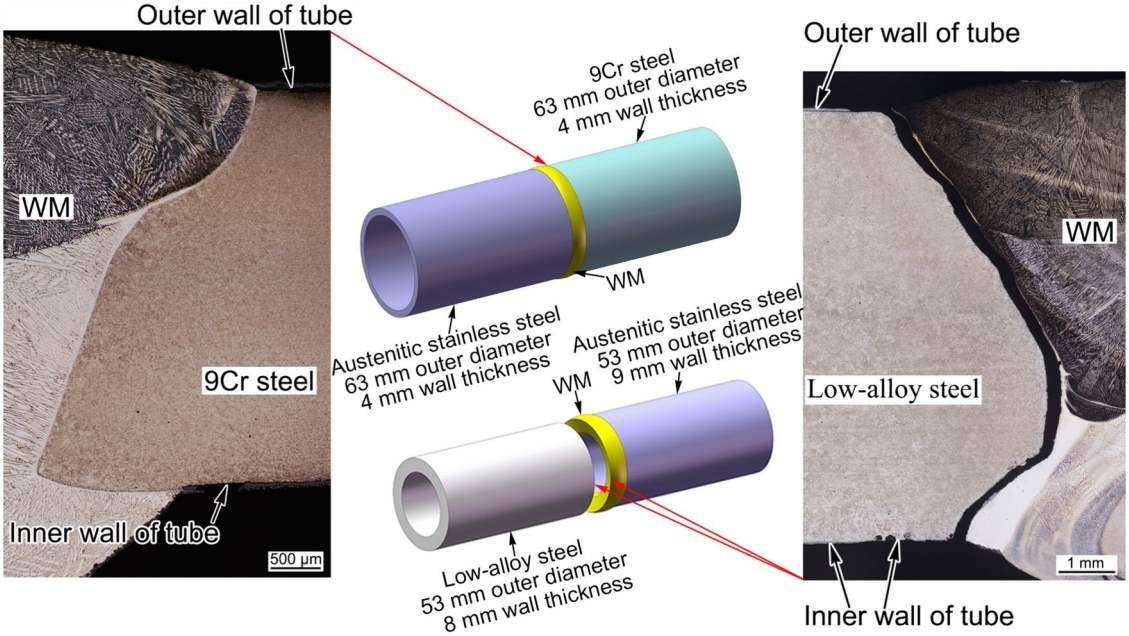

Figure 1 Cross-sectional images of the ferritic heat resistant steel side in the 9Cr steel DMW after service at 541 ℃ for 67000 h and in the low-alloy steel DMW after service at 541 ℃ for 15000 h [32]

evolution on the DMW service were analyzed, which provided theoretical support for further failure mechanism analysis. The premature failure of low-alloy steel DMW was the focus of this research, while 9Cr steel DMW was used for the comparative analysis. Therefore, different lengths of service time of 9Cr steel DMW and low-alloy steel DMW did not affect our concerns.

3.2 FEA Models and Service Simulation of Steam Tubes Containing DMWs

3.2.1 FEA Models of Steam Tubes Containing Low-alloy Steel DMW and 9Cr steel DMW

Numerical simulation method was used to obtain stress and strain evolution in the low-alloy steel DMW and in the 9Cr steel DMW during service. As shown in Figure 2, the FEA models containing low-alloy steel DMW (Figure 2a) and 9Cr steel DMW (Figure 2b) were built in accordance with the practical shape and dimension of

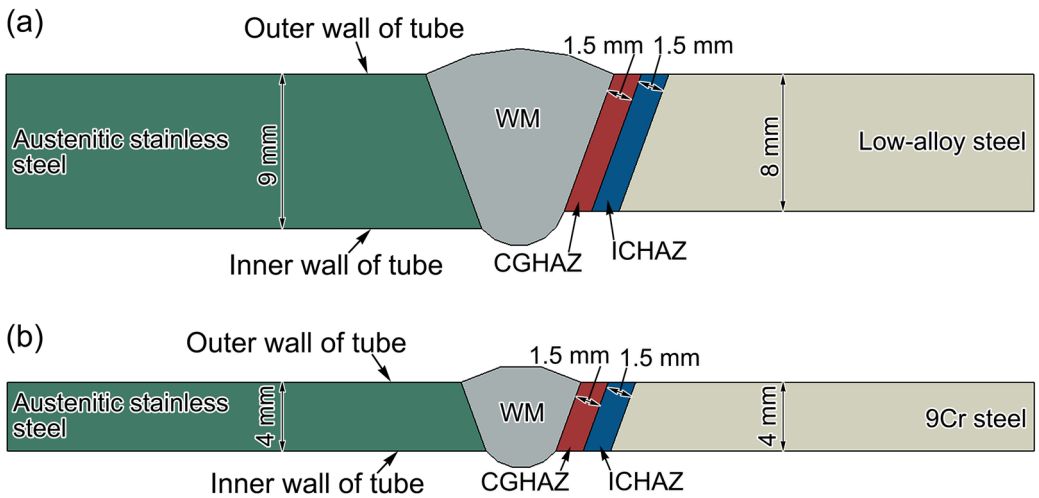

Figure 2 Axisymmetric FEA models for steam tubes contianing different DMWs: **a** Low-alloy steel DMW, **b** 9Cr steel DMW

DMWs in steam tubes. In order to simplify the simulation process, the axisymmetric model was adopted and the symmetry axis was the central axis of the tube. The nickel-based WM was located in the center of the model, and the two sides of the WM were ferritic heat resistant steel BM and austenitic stainless steel BM respectively. For DMWs, the damage and failure mainly occur on the ferritic heat resistant steel side and the austenitic stainless steel side was simplified without considering the existence of HAZ. The ferritic heat resistant HAZ was simplified into coarse-grained HAZ (CGHAZ) and intercritical HAZ (ICHAZ). The mesh of the BM was set to 1 mm to reduce the calculation burden. The HAZ and the vicinity of the WM/HAZ interface were the interested locations with the mesh of 0.1 mm. The local grid division was shown in Figure 3. The data of stress and strain were extracted along the specific paths, i.e. near the outer wall of the tube (paths 1 in Figure 3), in middle of the tube (paths 2 in Figure 3) and near the inner wall of the tube (paths 3 in Figure 3).

For DMWs, the thermal stress caused by the difference in CTE and the creep strain concentration caused by the difference in creep strength might be significant factor to degrade the mechanical properties. In order to consider the influence of thermal stress and creep strain respectively, the FEA was set up in three analysis steps. First, the tubes were heated to high-temperature. After the FEA calculation was completed, the thermal stress distribution in the DMW was extracted and analyzed. Then, the external load was applied. Finally, the long-term high-temperature service process was simulated, in which creep was considered. In the process of service, the temperature of steam inside the tube was 541 ℃. Meanwhile, there was the higher temperature flue gas outside the tube produced by coal combustion. In order to simplify the problem, the ambient temperature was set at 600 ℃ during FEA simulation. The radial load of the tube was the steam pressure. The axial force was applied by the axisymmetric model. Considering that the far end of the tube was blocked [33], the axial load needs to be set in the model. Based on the axial force balance of the tube section, the product of the area of steam flowing through tube section and the steam pressure should be equal to the product of the area between inner wall and outer wall of the tube and its axial stress of the tube. According to the calculation of the axial force balance of the tube section above, the axial load of low-alloy steel DMW tube was 16.6 MPa and that of 9Cr steel DMW tube was 11.2 MPa. During the simulation process of long-term service, one end of the tube was fixed and the other end was subjected to uniform tensile stress. The service simulation time of the low-alloy steel DMW tube was 15000 h, and the simulation time of the 9Cr steel DMW tube was 67000 h.

Norton's equation was employed to act as the creep constitutive relationship during long-term high-temperature service. The relationship between creep rate and stress is as follows:

$$\dot{\varepsilon} = A\sigma^n, \tag{1}$$

where $\dot{\varepsilon}$ is the creep rate, σ is the stress, and A and n are parameters related to the creep temperature. Table 1 shows the parameters of CTE, A and n used in FEA simulation. Other required material parameters were obtained from Refs. [27, 34–39]. It should be pointed out that the creep parameters of CGHAZ and ICHAZ were difficult to obtain. The creep strain rate of CGHAZ and ICHAZ was set as equal to corresponding ferritic BM and an order of magnitude higher than corresponding ferritic BM respectively [40, 41]. The simulation scheme used

Table 1 Material parameters at 600 ℃ [27, 34–39]

Material	A ($Pa^{-n}s^{-1}$)	*n*	CTE (K^{-1})
WM	4.98×10^{-79}	8.2	1.45×10^{-5}
9Cr steel	6.3×10^{-83}	9.1	1.26×10^{-5}
Austenitic stainless steel	5.36×10^{-94}	10.147	1.84×10^{-5}
Low-alloy steel	1.93×10^{-56}	6.02	1.39×10^{-5}

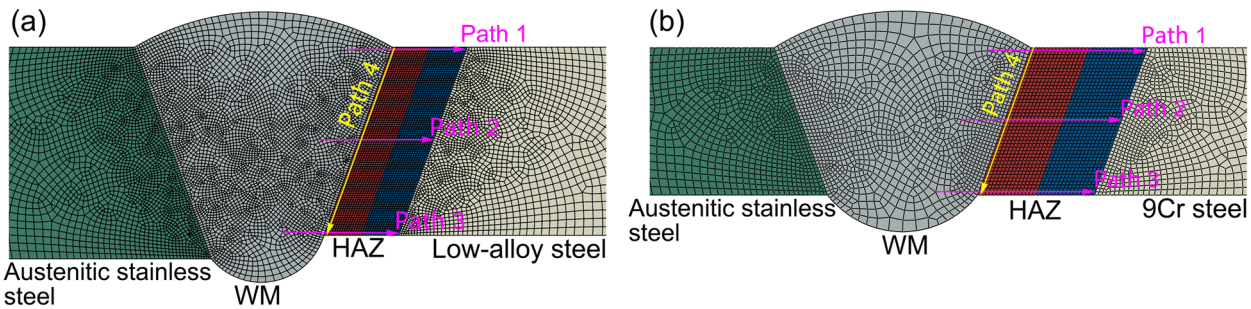

Figure 3 Mesh for DMWs and paths for extracting data: **a** Low-alloy steel DMW, **b** 9Cr steel DMW

has proved its validity in our previous study, and more details could be found in Ref. [42].

3.2.2 Experimental Validation of FEA Results

Before stress and strain analyses for the DMWs, the validity of the simulation results by FEA should be verified by experiment. Creep is the main mechanical damage form of the DMWs during long-term high-temperature service. Due to the difference in creep strength, creep strain concentration would be formed near the interface between nickel-based WM and ferritic heat resistant steel. According to FEA simulation results, the degree of interface creep strain concentration was different in different positions of tubes. After 15000 h of service simulation for the low-alloy steel DMW tube, the equivalent creep strain near the WM/HAZ interface was extracted along path 1 (Figure 3a), path 2 (Figure 3a) and path 3 (Figure 3a) respectively, as shown in Figure 4. There was an obvious equivalent creep strain concentration at the WM/HAZ interface near the inner wall of the tube and there was also an equivalent creep strain concentration at the WM/HAZ interface near the outer wall of the tube, while there was no obvious equivalent creep strain concentration at the WM/HAZ interface in the middle of the tube. Based on the FEA result, the creep damage characteristic of the tube was that the creep strain concentration was most serious at the WM/HAZ interface near the inner wall.

It has been reported that the characteristic parameters obtained by EBSD could reflect the deformation and damage of materials. Kamaya et al. [43] reported that Grain Reference Orientation Deviation (GROD) has a good linear relationship with plastic deformation.

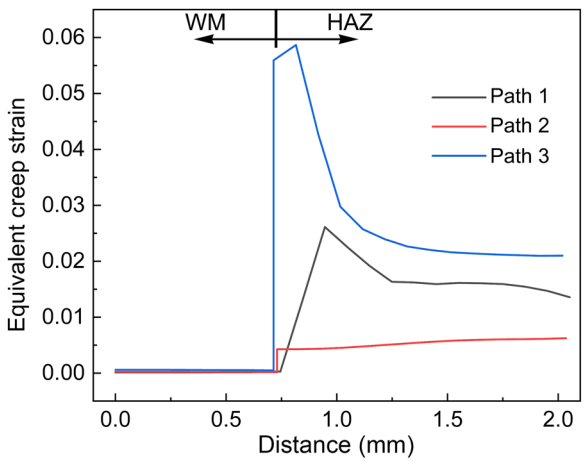

Figure 4 Equivalent creep strain profile along paths 1 ~ 3 in Figure 3a, in the low-alloy steel side of DMW after service simulaiton for 15000 h

Furthermore, Kobayashi et al. [44] and Rui et al. [45] believed that $\overline{\text{GROD}}$ has a linear relationship with creep deformation. In this study, EBSD was performed at the different positions in low-alloy steel DMW tube after service for 15000 h, and the creep deformation distribution near the WM/HAZ interface was evaluated by GROD. Figure 5 shows IPF and corresponding GROD maps for the nickel-based WM/low-alloy steel HAZ interface in the DMW after service for 15000 h. Near the inner wall of the tube, GROD at the WM/HAZ interface was significantly higher than other nearby regions, as shown in Figure 5c. Near the outer wall of the tube, GROD at the WM/HAZ interface was slightly higher than other nearby regions, as shown in Figure 5a. In the middle of the tube, GROD at the WM/HAZ interface did not increase significantly compared with other nearby regions, as shown in Figure 5b.

Further, the GROD data of the area shown in Figure 5 were extracted, which were averaged along the diameter direction of the tube, and the $\overline{\text{GROD}}$ distribution along the axis direction was obtained, as shown in Figure 6. According to the linear correlation of $\overline{\text{GROD}}$ and creep deformation, the creep strain was obviously high at the WM/HAZ interface near the inner wall of the tube and there was creep strain concentration at this position. There was also creep strain concentration at the WM/HAZ interface near the outer wall of the tube, but there was no obvious creep strain concentration at the WM/HAZ interface in the middle of the tube, as shown in Figure 6. The characteristics of interface creep strain concentration in the ex-service tube obtained by experiment were consistent with those obtained by FEA simulation, which verified the validity of the FEA model and its calculated results. The creep strain damage accumulation at the WM/ferritic steel interface was mainly determined by the creep gradient across interface and the difference in CTE between the austenitic material and ferritic material. The results in Section 3.2.2 meant that the FEA model whose main influence factor was the property of materials was reliable. Therefore, the experimental validation for the FEA model by the 9Cr steel DMW was omitted.

3.2.3 Stress and Strain Evolution in Low-alloy Steel DMW and 9Cr Steel DMW During Service

Figure 7 shows the Mises stress distributions in the DMWs when the tubes were heated to 600 ℃ without load, and the stress was only caused by the thermal expansion of the materials. There was stress concentration at the WM/steel interface in low-alloy steel DMW and in 9Cr steel DMW, and the most serious stress concentration was near the inner and outer walls. For low-alloy steel DMW, the Mises stress at the WM/austenitic

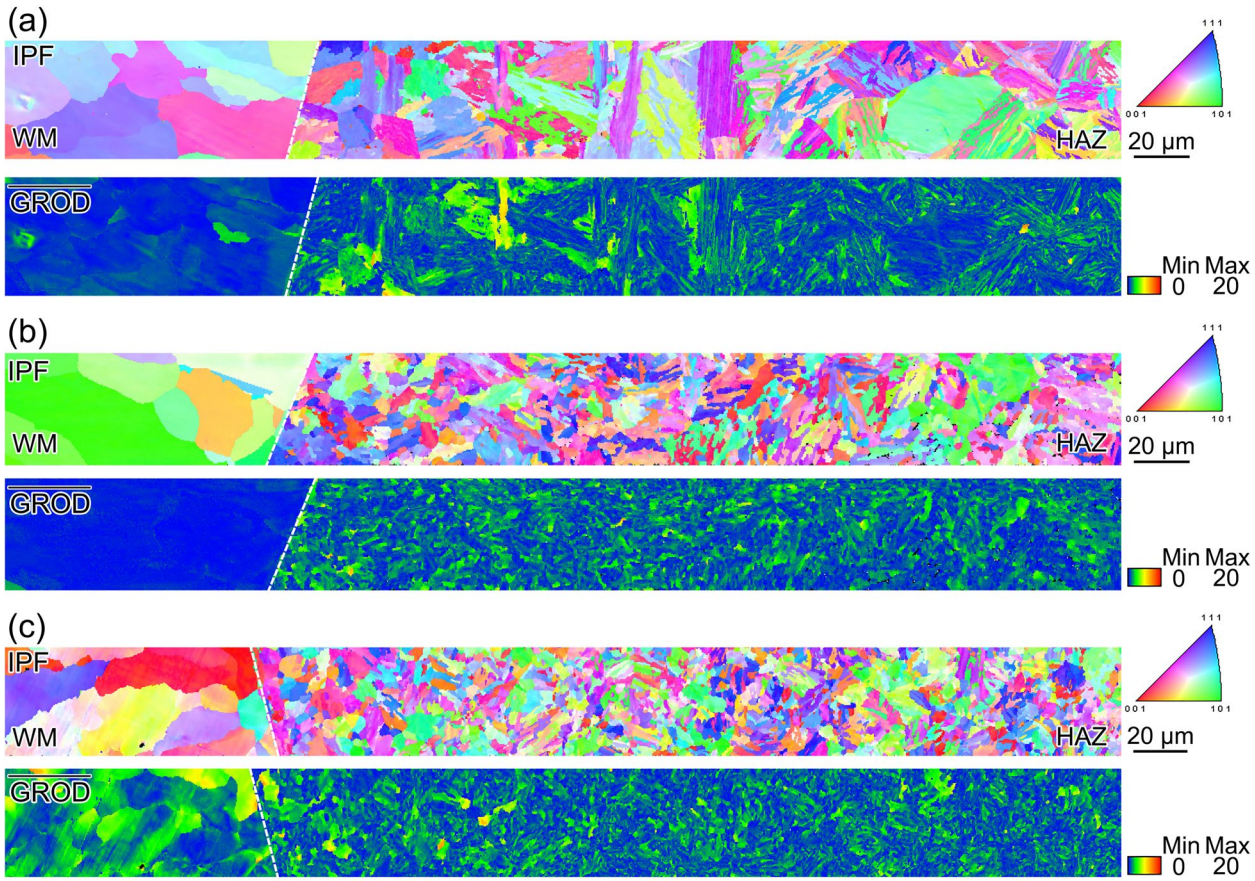

Figure 5 IPF and corresponding GROD maps of the low-alloy steel side of the ex-service DMW operated at 541 ℃ steam temperature for 15000 h: **a** Near the outer wall of the tube, **b** In middle of the tube, **c** Near the inner wall of the tube

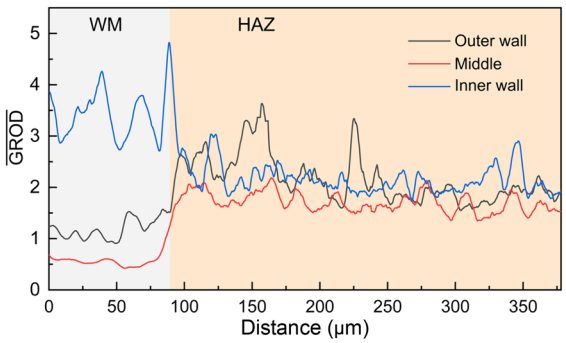

Figure 6 $\overline{\text{GROD}}$ profile o of the low-alloy steel side of the ex-service DMW operated at 541 ℃ steam temperature for 15000 h

steel interface was up to 249 MPa near the outer wall, the Mises stress at the WM/austenitic steel interface was up to 250 MPa near the inner wall, the Mises stress at the WM/ferritic steel interface was up to 180 MPa near the outer wall, and the Mises stress at WM/ferritic steel interface was up to 155 MPa near the inner wall. In comparison with the WM/austenitic steel interface, the lower thermal stress at the WM/ferritic steel interface was related to the small difference in CTE between WM and ferritic steel. For 9Cr steel DMW, the Mises stress in the austenitic steel side was up to 282 MPa and it in the 9Cr steel side was up to 215 MPa.

The ex-service low-alloy steel DMW ruptured in the low-alloy steel side after 15000 h service, so the creep strain distribution in the low-alloy steel side after 15000 h service of DMW was obtained by FEA simulation to analyse the influence of creep strain on failure. Figure 8 shows the equivalent creep strain distribution in the low-alloy steel DMW after 15000 h service simulation. The equivalent creep strain was mainly concentrated in the low-alloy steel side due to its poor high temperature deformation resistance. The WM and the austenitic steel side without obvious creep deformation were due to their high creep resistance. There was creep strain concentration at the WM/low-alloy steel interface near the tube walls, while the creep strain concentration at the WM/low-alloy steel interface in the middle of the tube was not obvious, which was related to the different restrain. Laha et al. [11] pointed out that the nickel-based WM would

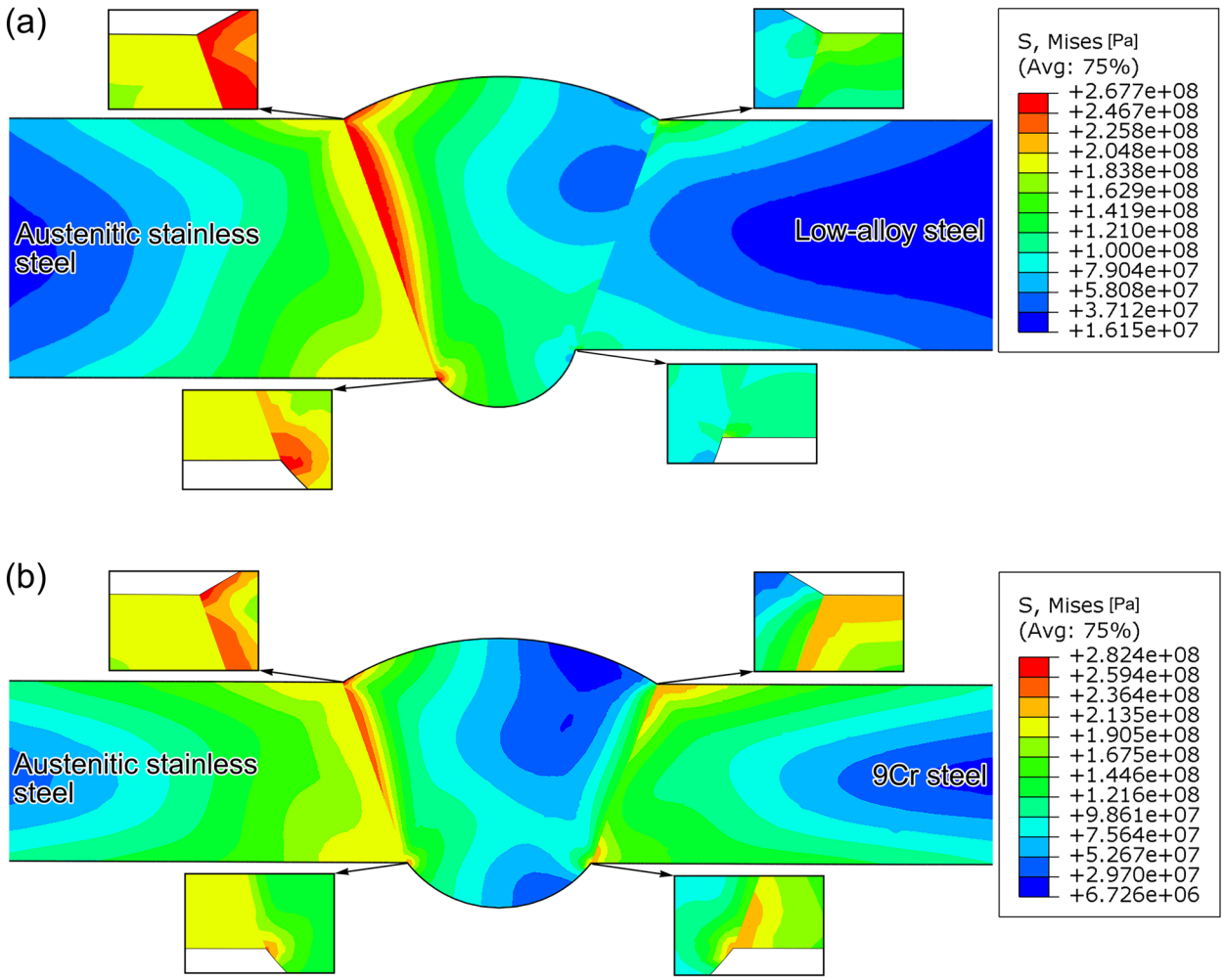

Figure 7 Mises stress distributions of different DMWs, in which only temperature field was applied: **a** Low-alloy steel DMW, **b** 9Cr steel DMW

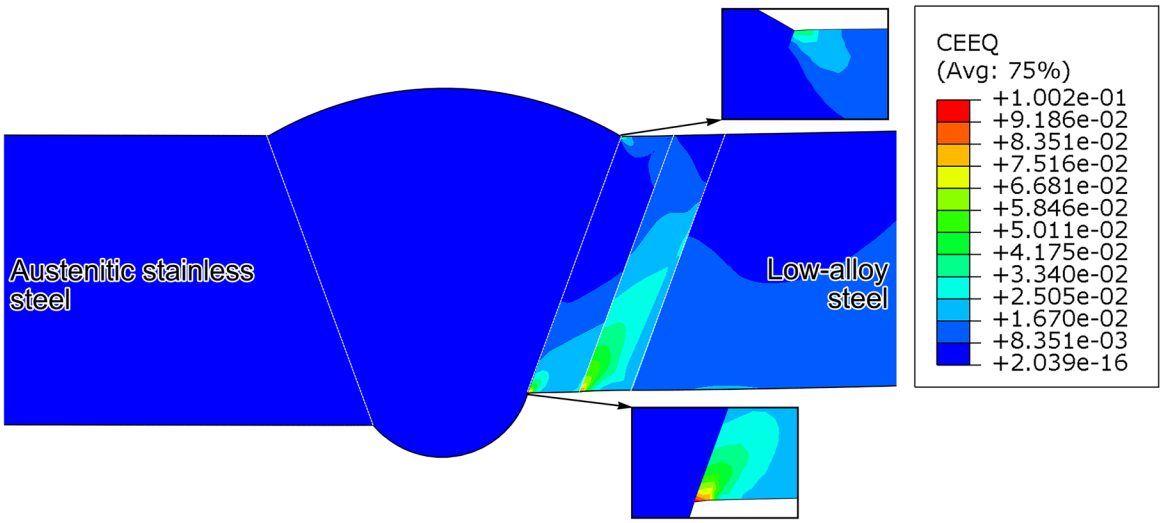

Figure 8 Equivalent creep strain distribution of low-alloy steel DMW after service simulation for 15000 h

constrain the deformation of its nearby HAZ, and the restrain degree inside the sample was greater than that on the surface of the sample. Meanwhile, there was also high equivalent creep strain at the CGHAZ/ICHAZ interface near the inner wall of the tube, but the actual failure did not occur at this location, which implied that there were other key factors triggering the DMW interface failure in addition to mechanical factors.

The ex-service low-alloy steel DMW ruptured in the low-alloy steel side after 15000 h service, while the ex-service 9Cr steel DMW did not fail after 67000 h service. The creep strain concentration in DMWs contributed to the failure, which was related to the different properties on both sides of the WM/ferritic steel interface due to different materials. Thus, the creep strain distribution in the 9Cr steel side after 67000 h service of 9Cr steel DMW was obtained by FEA simulation to analyse the difference of creep strain distribution between the two ex-service DMWs and the contribution of creep strain concentration to failure. Figure 9 shows the equivalent creep strain distribution in the 9Cr steel DMW after 67000 h service simulation. There was creep strain concentration at the WM/HAZ near the tube walls, while the creep strain concentration at the WM/HAZ interface in the middle of the tube was not obvious. In particular, there was no obvious creep strain concentration at the CGHAZ/ICHAZ interface in the 9Cr steel DMW.

Figure 10 shows the Mises stress distribution in DMWs after long-term service simulation. The maximum Mises stress in the low-alloy steel DMW was up to 180 MPa and was located at the WM/low-alloy steel interface near the outer wall of the tube, as shown in Figure 10a, and the stress concentration there would promote the interface cracking. The Mises stress at the WM/austenitic steel interface was highest when the temperature field was applied only, as shown in Figure 7a. After long-term service, obvious creep deformation occurred in the low-alloy steel side of the DMW and thus the stress in the austenitic steel side was released. Figure 10b shows the Mises stress distribution in 9Cr steel DMW after 67000 h service simulation, and the maximum Mises stress in the whole DMW was only 117 MPa.

3.2.4 Quantitative Analyses of Stress and Strain Near WM/HAZ Interface During Service

The strain and stress in the DMWs were further analyzed quantitatively. The equivalent creep strain and Mises stress in the low-alloy steel DMW were extracted along path 1, path 2 and path 3 in Figure 3a. Near the outer wall of the low-alloy steel DMW tube, strain concentration at the WM/low-alloy steel interface became more and more serious with the extension of service time, as shown in Figure 11a. Meanwhile, Mises stress concentration appeared at the WM/low-alloy steel interface, as shown in Figure 11b. In the middle of the low-alloy steel DMW tube, there were equivalent creep strain and Mises stress steps existed at the WM/HAZ interface and the CGHAZ/ICHAZ interface, as shown in Figure 11c and d, but no obvious creep strain or stress concentration was observed. Near the inner wall of the low-alloy steel DMW tube, there was creep strain concentration at the WM/HAZ interface and the CGHAZ/ICHAZ interface, as shown in Figure 11e, and equivalent creep strain at the WM/HAZ interface and the CGHAZ/ICHAZ interface was up to 5.86% and 7.68% after 15000 h respectively. However, the Mises stress at the WM/HAZ interface and the CGHAZ/ICHAZ interface only showed a step without significant concentration, as shown in Figure 11f.

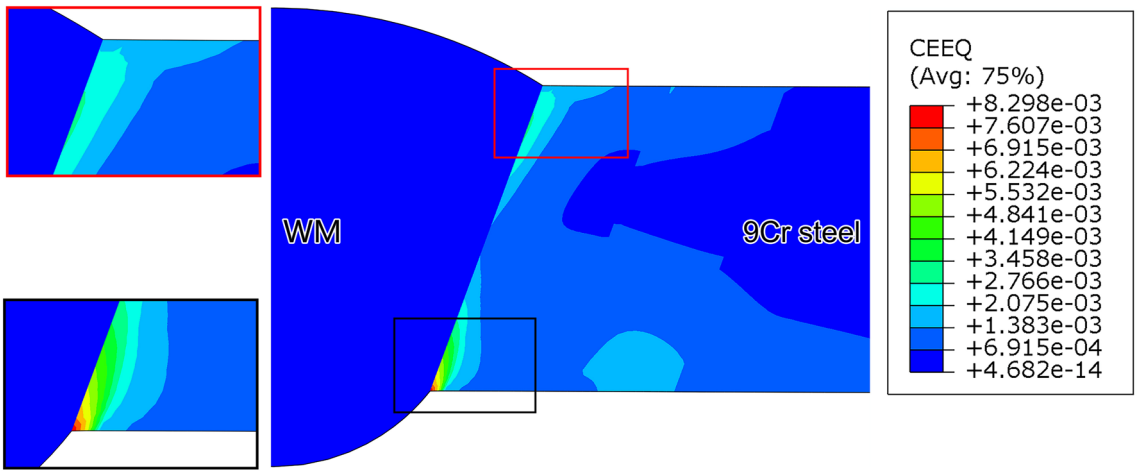

Figure 9 Equivalent creep strain distribution of 9Cr steel DMW after service simulation for 67000 h

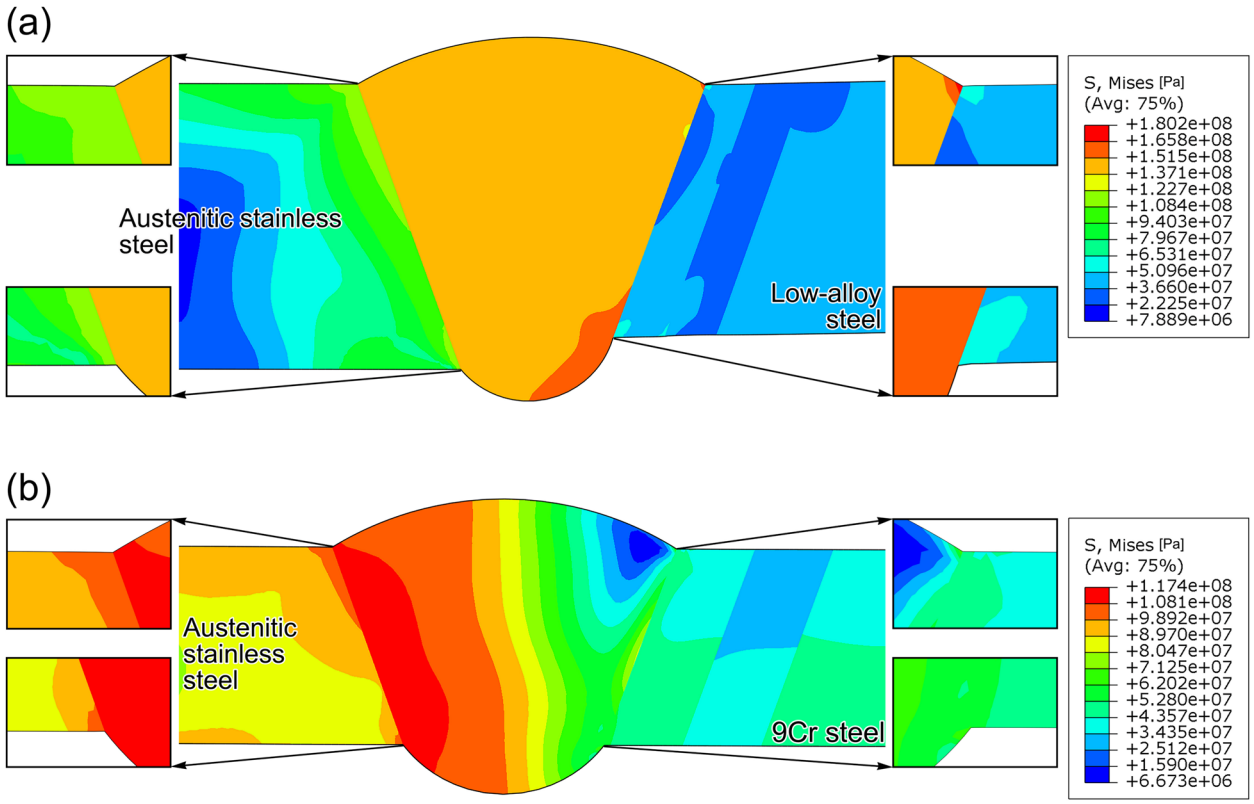

Figure 10 Mises stress distributions of different DMWs after service simulation: **a** Low-alloy steel DMW after 15000 h, **b** 9Cr steel DMW after 67000 h

The equivalent creep strain and Mises stress were extracted along path 4 in Figure 3a, and the results are shown in Figure 12. After 15000 h of service simulation, the equivalent creep strain at the WM/low-alloy steel interface of the outer wall was 4.08%, and that of the inner wall was 8.34%, as shown in Figure 12a. Compared with the thermal stress caused by only considering the difference in CTE, the Mises stress at the WM/low-alloy steel interface of the outer wall and that of the inner wall decreased by about 67% and 63% after 15000 h, as shown in Figure 12b.

The equivalent creep strain and Mises stress in the 9Cr steel DMW were extracted along path 1, path 2 and path 3 in Figure 3b, and the results are shown in Figure 13. For the 9Cr steel DMW tube, there was a certain degree of creep strain concentration at WM/9Cr steel interface, and the interface creep strain increased gradually with the extension of service time. It is worth noting that with the extension of service time, the Mises stress at the WM/9Cr steel interface and in the whole HAZ decreased significantly, indicating that the creep deformation would greatly alleviate the stress concentration in the 9Cr steel DMW.

The equivalent creep strain and Mises stress were extracted along path 4 in Figure 3b, and the results are shown in Figure 14. After 67000 h of service simulation, the creep deformation at WM/9Cr steel interface near the inner wall of the tube was most obvious, as shown in Figure 14a. Compared with the thermal stress caused by only considering the difference in CTE, the Mises stress at the WM/9Cr steel interface of the outer wall and that of the inner wall decreased by about 82% and 75% after 67000 h, as shown in Figure 14b.

According to the above FEA results, the stress and strain in the ferritic/austenitic DMWs of tubes were clarified. Whether the low-alloy steel DMW or 9Cr steel DMW, with the increase of service time, the creep strain at nickel-based WM/ferritic heat resistant steel interface continued to be accumulated, and there was creep strain concentration at the interface near the outer wall and inner wall of the tube. The Mises stress in the DMW decreased after creep deformation, which was related to stress release caused by strain. The accumulation of creep deformation had different effects on the interface stress distributions in the low-alloy steel DMW tube and the 9Cr steel DMW

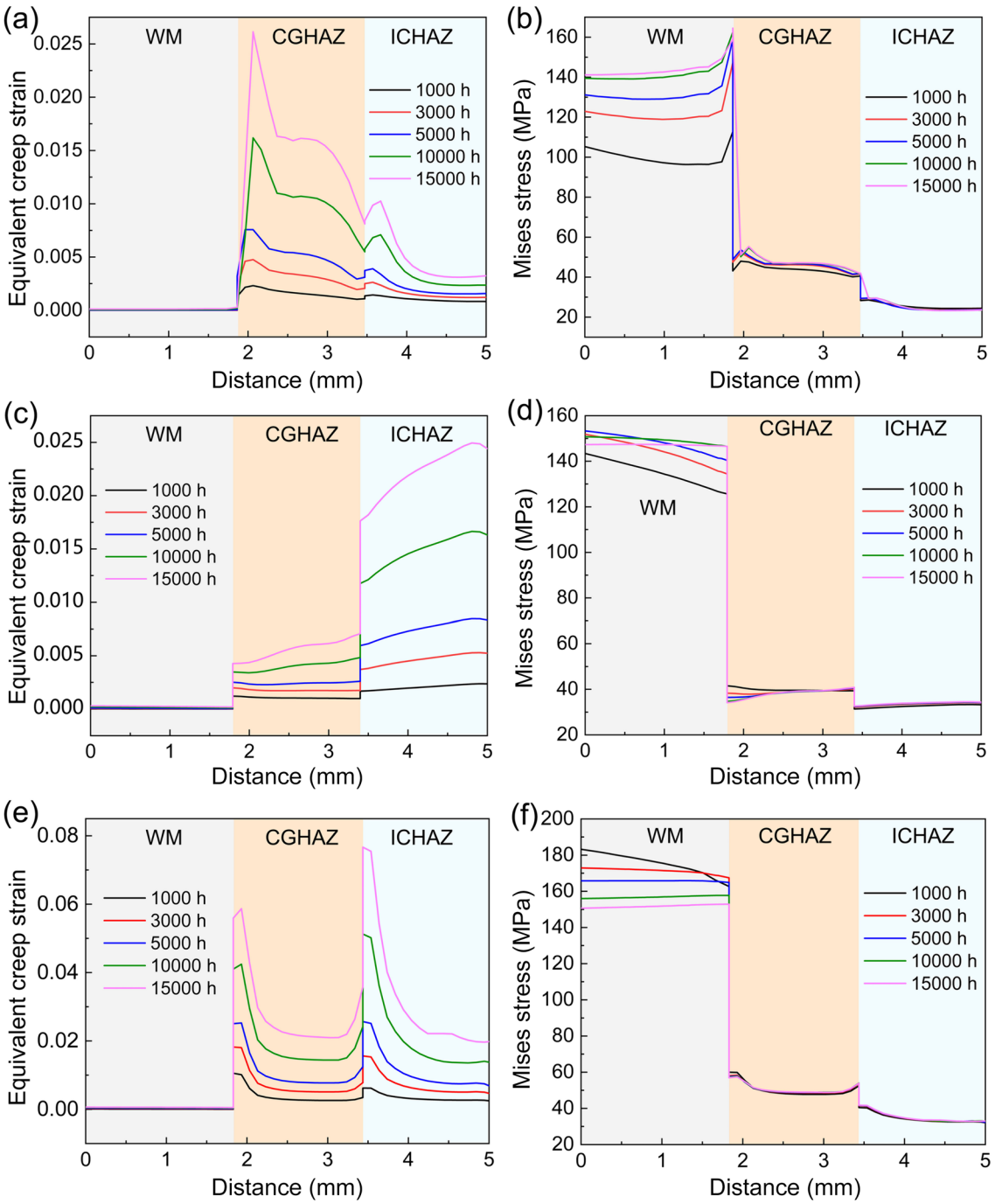

Figure 11 Equivalent creep strain and Mises stress distributions of the low-alloy steel side of the DMW after different service simulation time along the paths in Figure 3a: **a** and **b** Along path 1, **c** and **d** Along path 2, **e** and **f** Along path 3

tube. With the extension of service time, the Mises stress at the WM/low-alloy steel interface near the outer wall of the low-alloy steel DMW tube increased continuously, while the Mises stress at WM/9Cr steel interface decreased continuously in the 9Cr steel DMW tube.

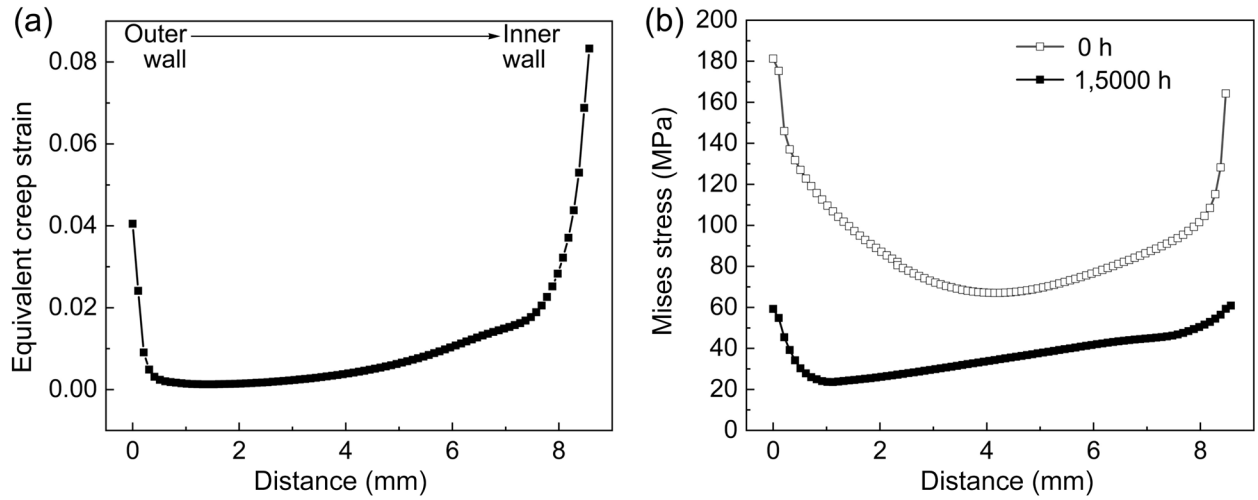

Figure 12 Equivalent creep strain and Mises stress along the WM/low-alloy steel interface in the DMW: (**a**) Equivalent creep strain distribution along path 4 in Figure 3a in the DMW after service simulation for 15000 h, (**b**) Mises stress distribution along path 4 in Figure 3a in the DMW after service simulation for 0 h and 15000 h

3.3 Analyses of Failure Mechanism of DMWs by the Combination of Microstructure, Oxidation and Mechanics Factors

In Section 3.2, the effect of strain and stress evolution in the DMWs has been considered by simulation method. However, there were microstructure evolution and oxidation occurred in DMWs in power plants, which could affect the DMW failure. In Section 3.3, microstructure, oxidation and mechanics factors were considered simultaneously to reveal the failure mode and mechanism of the DMW.

3.3.1 Effect of Microstructure on Interface Failure

The DMW premature failure was closely related to the interfacial microstructure There was a martensite layer with 1 ~ 3 μm width formed along the nickel-based WM/ferritic HAZ interface due to different materials welding [46]. Our previous research has shown that the interface microstructure would be degraded during long-term service [29], as shown in Figure 15. During long-term high-temperature service, the part of the martensite layer adjacent to WM degraded into ferrite, while the other part of it adjacent to HAZ transformed into carbide precipitation region, and above microstructure evolution was dominated by carbon diffusion induced by large carbon chemical potential gradient on both sides of the interface. In both the low-alloy steel DMW and 9Cr steel DMW, the above microstructure evolution occurred along the interface between the nickel-based WM and ferritic HAZ. In the ex-service low-alloy steel DMW and 9Cr steel DMW, the interface ferrite band formed due to long-term service was marked by white arrows in Figure 15a and c, and the carbide precipitation region was marked by yellow arrows in Figure 15a and c. By creep tests, we proved that the newly formed ferrite band along the interface was prone to crack, as marked by white arrows in Figure 15e, contributing to the macroscopic interface failure of DMW. In turn, some mechanistic changes had a promoting effect on interfacial microstructure evolution. The literature shows the hardness of ferritic HAZ was higher than that of nickel-based WM and ferritic BM due to the quench hardening structures, and this mechanistic feature cannot be changed by long-term service [32]. The difference in hardness on both sides of the WM/ferritic steel interface would cause the deformation to concentrate at the interface during long-term service, which promoted the microstructure evolution at the WM/ferritic steel interface. In addition, welding residual stress [47] and inhomogeneity caused by interfacial microstructure [48] were also thought to contribute to DMW failure.

The promoting effect of interface ferrite on DMW failure was during service, however, it is not clear whether there is a significant effect of interface ferrite on the macroscopic mechanical properties of the DMW. In this section, high-temperature tensile tests were conducted on the low-alloy steel DMW before service, the low-alloy steel DMW in the steam tube after service for 15000 h in power plant, and the 9Cr steel DMW in the steam tube after service for 67000 h in power plant.

Due to the thin wall thickness of the tube, small tensile samples were employed. The dimension of the tensile sample is shown in Figure 16. The tensile tests were conducted at 600 ℃ and the tensile rate was 1.0×10^{-3}/s.

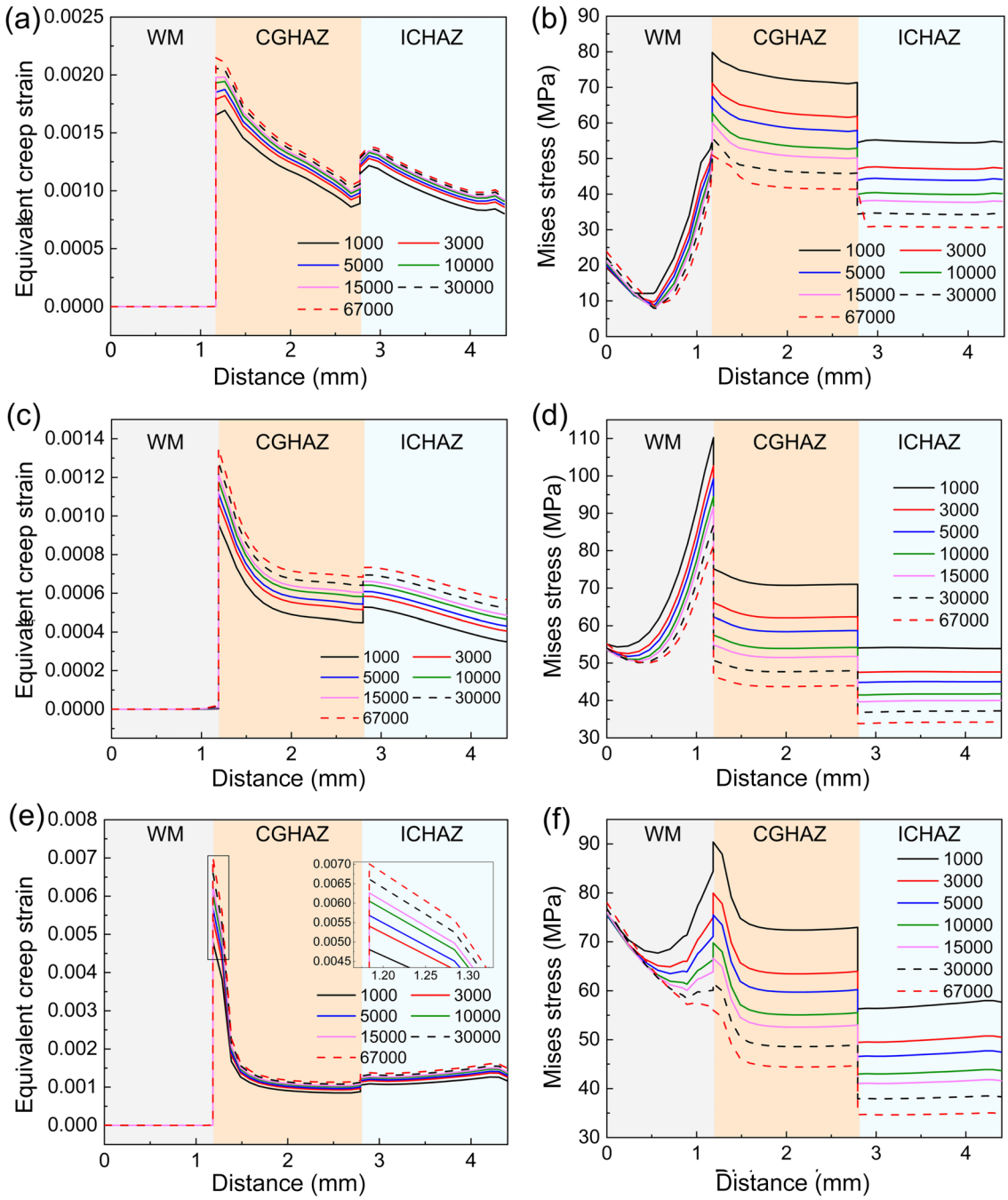

Figure 13 Equivalent creep strain and Mises stress distributions of the 9Cr steel side of the DMW after different service simulation time along the paths in Figure 3b: **a** and **b** Along path 1, **c** and **d** Along path 2, **e** and **f** Along path 3

Repeated experiments were performed to ensure that the data were reliable.

Table 2 shows the tensile properties of different DMWs. The yield strength (*YS*) of the low-alloy steel DMW before service was 211.78 MPa and the *YS* of the low-alloy steel DMW after service was 214.9 MPa, which indicated that the *YS* of the low-alloy steel DMW was not changed significantly by the long-term service. However, the ultimate tensile strength (*UTS*) of the low-alloy steel DMW has decreased by about 33 MPa after long-term service. The elongation to failure (δ) and the reduction of sample area (Ψ) could represent the plasticity. The δ and Ψ of the low-alloy steel DMW before service were 14.7% and 68.82% respectively, and the δ and Ψ of the low-alloy

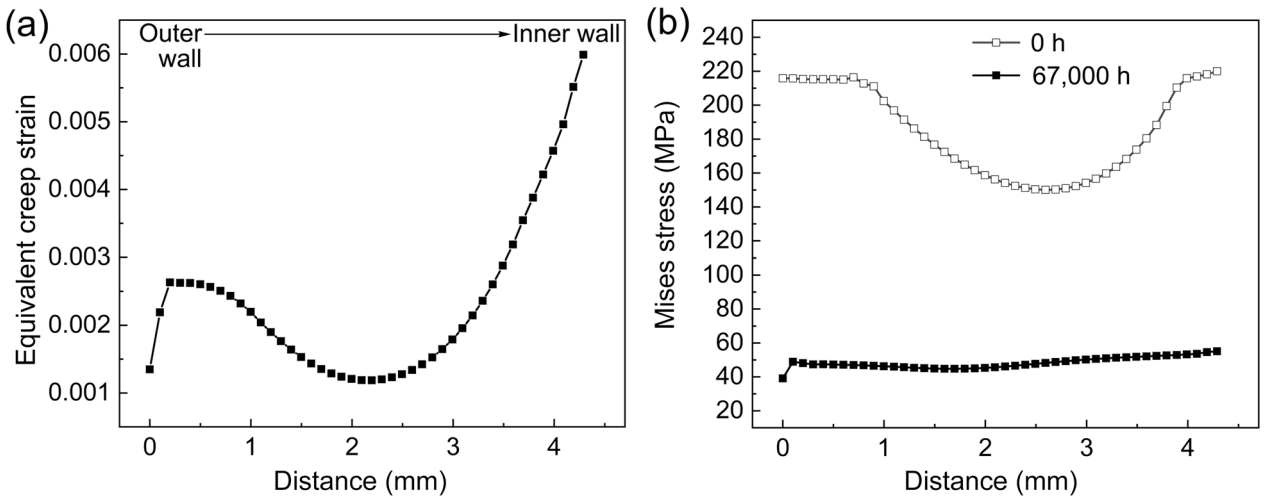

Figure 14 Equivalent creep strain and Mises stress along the WM/9Cr steel interface in the DMW: **a** Equivalent creep strain distribution along path 4 in Figure 3b in the DMW after service simulation for 67000 h, **b** Mises stress distribution along path 4 in Figure 3b in the DMW after service simulation for 0 h and 67000 h

steel DMW after service were 10.24% and 55.63% respectively. The δ and Ψ of the low-alloy steel DMW decreased after service, which indicated the plasticity of the low-alloy steel DMW was reduced due to long-term service. The *YS* of the 9Cr steel DMW after service was still 216.46 MPa, and the *UTS* of it was still 346.92 MPa. Figure 17 shows the stress-strain curves of the DMWs during the tensile tests at 600 ℃. Compared with the low-alloy steel DMW before service, the flow stress of the ex-service low-alloy steel DMW increased during tensile testing, but the failure strain decreased, which also indicated that the long-term service made the low-alloy steel DMW harden to a certain extent. The flow stress of 9Cr steel DMW was higher than that of low-alloy steel DMW.

Figure 18 shows the crack profiles of the broken samples after tensile tests, and the failure locations were observed by OM. The failure locations of the three types of DMWs were far away from the WM/ferritic steel interface. The fibrous microstructure caused by plastic flow could be observed near the fracture path of the low-alloy steel DMW before service, the low-alloy steel DMW after service, and the 9Cr steel DMW after service, as shown in Figure 18, which indicated that the tensile failure was dominated by plastic deformation. Figure 19 shows the fracture appearance of the low-alloy steel DMW before service and the low-alloy steel DMW after service. The fracture appearance of low-alloy steel DMW before service showed obvious neck deformation, as shown in Figure 19a, and it was composed of a dimple with a large size, as shown in Figure 19b. There was no obvious neck deformation of the fracture appearance of low-alloy steel DMW after service, as shown in Figure 19c, the dimple size on the fracture appearance was also small, as shown in Figure 19d. The results of fracture appearance observation were consistent with the results of tensile properties, and both showed that the long-term service would reduce the plasticity of the DMW. Under tensile loading conditions, the three types of DMWs were broken in the ferritic steel BMs. Nickel-based WM and austenitic BM have excellent high-temperature performance. The hardness of the ferritic CGHAZ was higher than that of the ferritic BM due to the welding thermal cycle. The hardness of the ferritic ICHAZ was usually low [26], but its deformation would be constrained by the nickel-based WM and CGHAZ, resulting that it was not easy to deform [47]. As a result, a large range of plastic deformation occurred in the unconstrained ferritic BM, and the failure of DMW eventually occurred in ferritic BM. According to the high-temperature tensile test results of the DMWs, the degraded interface microstructure could trigger the interface failure of DMW only under the long-term service of low stress conditions.

3.3.2 Effect of Oxidation on Interface Failure

The interface premature failure of DMW was also closely related to the oxidation. Meanwhile, the interface oxidation was affected by interfacial microstructure. To confirm the effect of interface microstructure and oxidation on interface failure, the ex-service 9Cr steel DMW was taken from an ex-service tube after service for 80000 h in practical power plant. The interface between nickel-based WM and 9Cr steel was observed by SEM, as shown in Figure 20. Type I carbides existed along the interface. There was also a ferrite band with a width of about 500

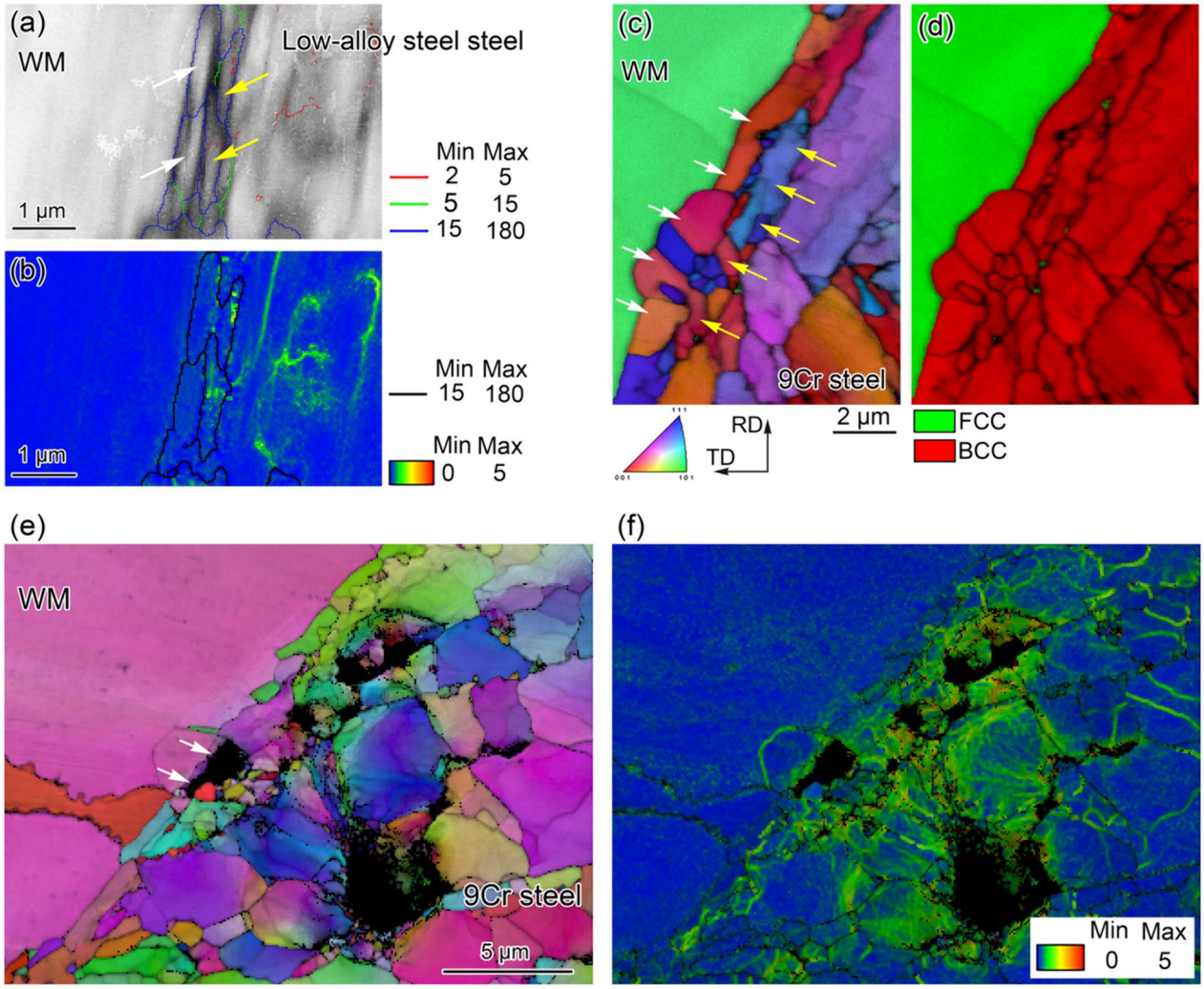

Figure 15 Interfacial microstructure and its effect on creep failure, revealed by EBSD [29]: **a** Boundary figure (BF) + image quality (IQ) map and **b** Kernel average misorientation (KAM) + BF map, located near the WM/low-alloy steel interface in the DMW after long-term service in power plant; **c** Inverse pole figure (IPF) + IQ map and **d** Phase + IQ map, located near the WM/9Cr steel interface in the DMW after long-term service in power plant; **e** IPF + IQ map and **f** KAM + IQ map, located near the WM/9Cr steel interface in the DMW after creep test

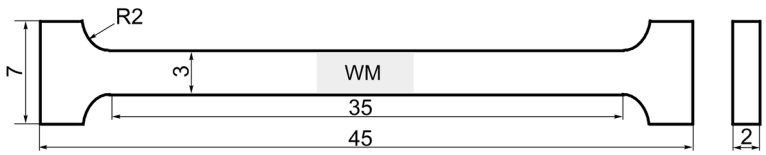

Figure 16 Dimension of DMW specimen for high-temperature tensile test (mm)

Table 2 Tensile properties of DMWs at 600 ℃

Materials	State	*YS*(MPa)	*UTS*(MPa)	*Δ*(%)	*Ψ*(%)
Low-alloy steel DMW	Before service	211.78	343	14.70	68.82
	After service	214.9	309.98	10.24	55.63
9Cr steel DMW	After service	216.46	346.92	14.26	66.98

nm formed along the WM/ferritic steel interface, as marked by yellow arrows in Figure 20.

It was found that there was a crack of approximately 300 μm in length along the nickel-based WM/9Cr steel interface on the outer wall of the 9Cr steel DMW tube after service for 80000 h, as shown in Figure 21a. The

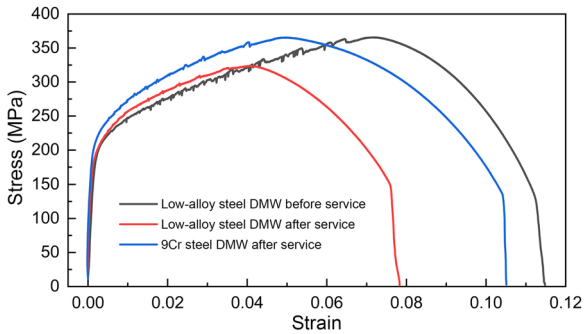

Figure 17 Representative engineering stress–true strain curves of DMWs

length of crack embedded in the matrix was far beyond the oxide layer thickness on the surface, meaning that it was not only oxidation along the interface but also accompanied by cracking along the interface. Figure 21b shows a high-magnification SEM image of the interface crack tip. The crack path had been oxidized, but traces of cracking could still be observed ahead of the oxidation, as indicated by the yellow arrow in Figure 21b. In particular, the cracking was along the interface ferrite band. Figure 21c shows BSE image of the interface crack tip. Figure 21d shows O element distribution and Figure 21e shows Cr element distribution, corresponding to Figure 21c. The O element distribution clearly showed the oxidized region. It is worth noting that there were some Cr rich locations along the crack path, as indicated by the red arrows in Figure 21e, and these Cr rich locations were type I carbides. There were some Cr poor locations along the crack path, as indicated by the black arrows in Figure 21e, which made oxidation more likely to occur along the interface. The above results show that the failure actually occurred along the interfacial ferrite band between the type I carbide region and the WM. In addition, no creep voids were observed around type I carbides region far from the crack tip. Therefore, the interfacial ferrite band was prone to crack during service, accompanied by the oxidation of crack tip, contributing to interface failure. It could be inferred that the interfacial

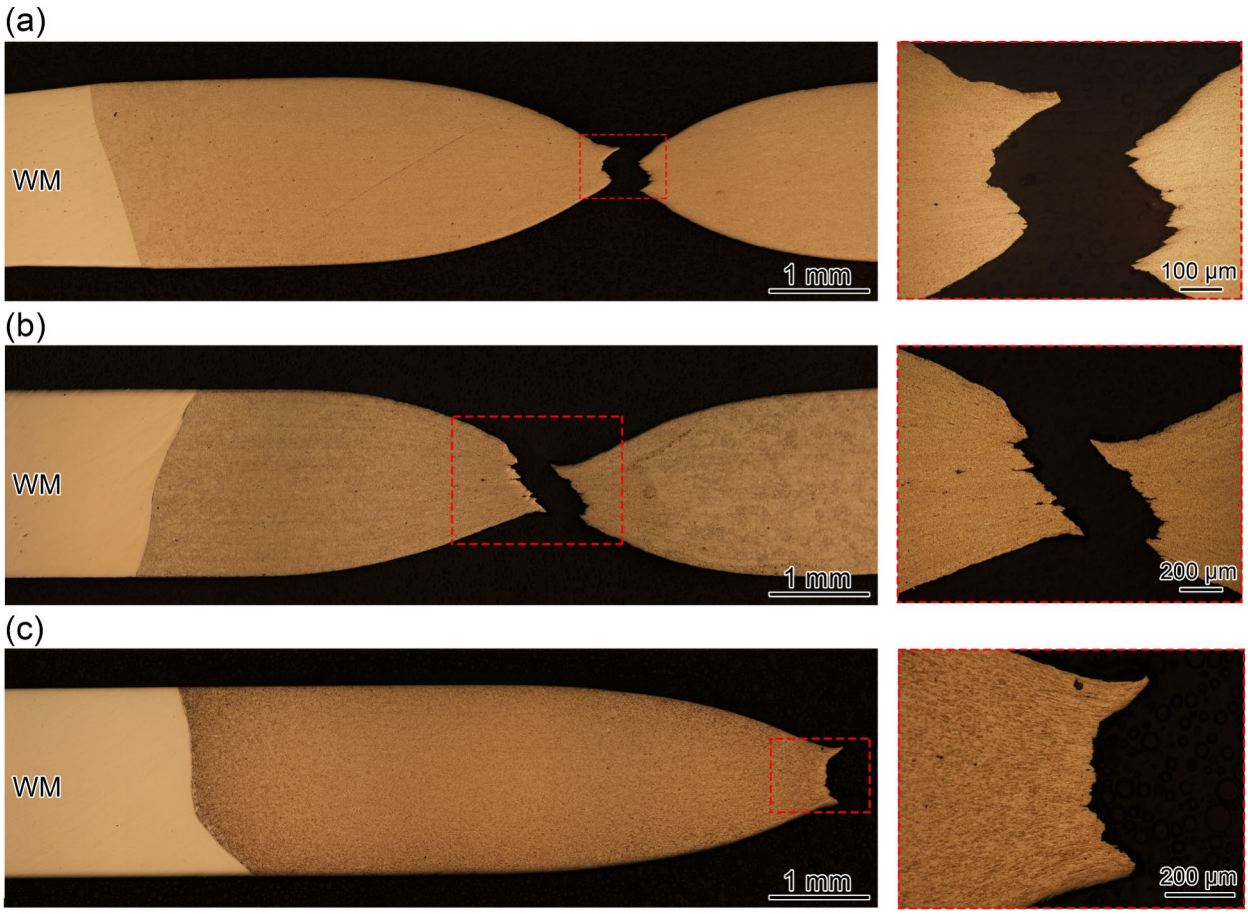

Figure 18 OM images near the fracture paths of the DMWs after high-temperature tensile tests: **a** Low-alloy steel DMW before service, **b** Low-alloy steel DMW after service for 15000 h, **c** 9Cr steel DMW after service for 67000 h

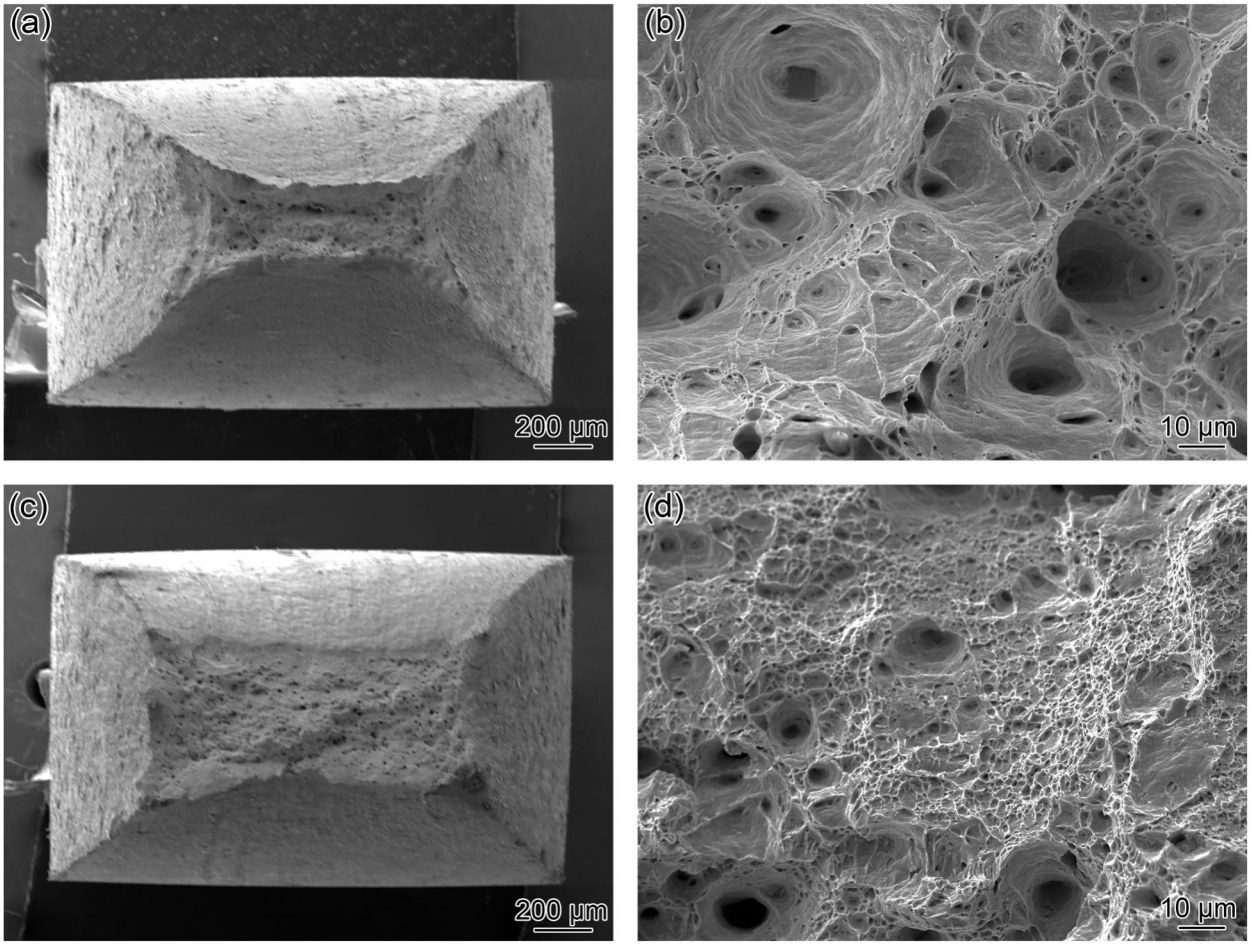

Figure 19 Fracture appearance of broken samples after high-temperature tensile tests: **a** Low-magnification SEM image of low-alloy steel DMW before service, **b** High-magnification SEM image of low-alloy steel DMW before service, **c** Low-magnification SEM image of low-alloy steel DMW after service, **d** High-magnification SEM image of low-alloy steel DMW after service

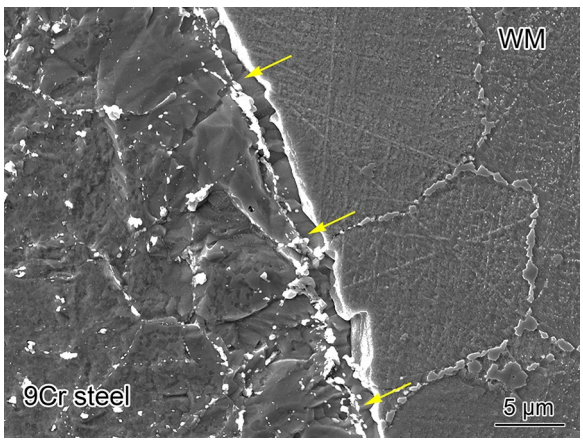

Figure 20 Interface microstructures of 9Cr steel DMW operated at 570 ℃ steam temperatur and 25 MPa steam pressure for 80000 h in power plant

ferrite band could have acted as channels for oxygen diffusion and led to interfacial oxidation. There was radial deformation between ferritic steel and nickel-based WM when the DMW was loaded, and thus there was uncoordinated deformation between the oxidized metal and the surrounding matrix, resulting in the oxide separation or falling off [26]. Furthermore, the oxidized ferrite band was prone to cracking. Meanwhile, the interfacial oxidation also intensified the interface cracking.

3.3.3 Interface Failure Mechanism of DMW in Power Plant

Based on the above results and discussion, the premature failure mode and mechanism of DMWs were clarified under actual service conditions in power plants, and the process is shown in Figure 22. During long-term service, the ferrite band was formed along nickel-based WM/ferritic heat resistant steel interface, which promoted interface oxidation, as shown in Figure 22a. The formation of ferrite band made the WM/ferritic steel interface

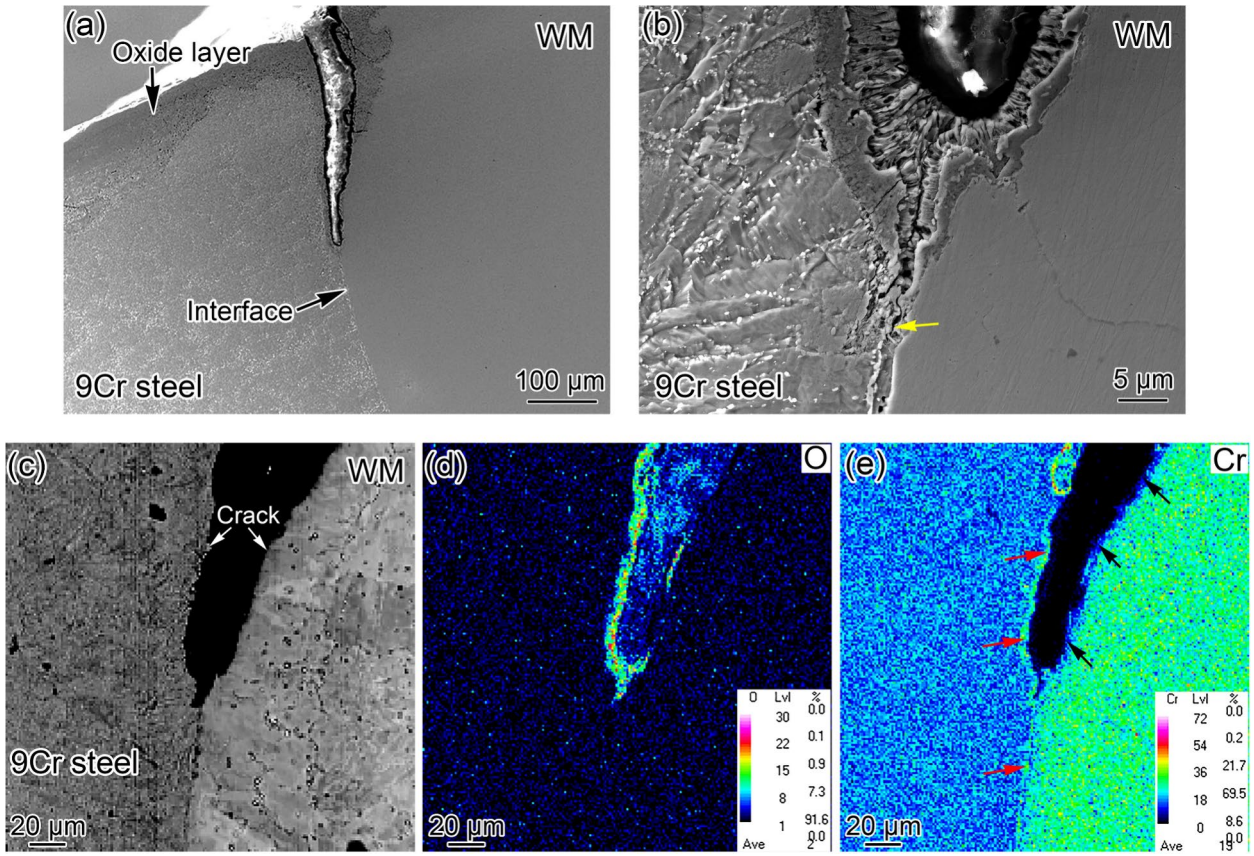

Figure 21 Crack along the WM/9Cr steel interface in the DMW after service for 80,000 h: **a** Interface crack; **b** Detailed SEM image of interface crack, **c** Backscattered electron (BSE) image of crack tip, **d** O element distribution, obtained by EPMA mapping and corresponded to (**c**), (**e**) Cr element distribution, obtained by EPMA mapping and corresponded to (**c**)

a weak position in the DMW. The difference in CTE and creep strength between the nickel-based WM and ferritic steel on both sides of the interface, the presence of the hardened HAZ, and the additional stress caused by the steam pressure in interior of the tube would introduce significant stress concentration at the WM/ferritic steel interface. As a result, there was significant strain concentration at the interface. In addition, the stress concentration ahead of the interface oxidation tip was more obvious, so the interface ferritic band would be cracked during service, as shown in Figure 22b. The interface crack was the early stage of failure, which would trigger fracturing along the WM/ferritic steel interface. After the formation of interface crack, high-temperature oxygenated atmosphere would enter the interface, and oxidation along the interface would continue to occur, as shown in Figure 22c. As oxides were easily broken, they would be separated from nearby metals under the action of interface stress, and cracking continued to occur near the interface, as shown in Figure 22d. Finally, macroscopic failure occurred along the WM/ferritic steel interface. It should be pointed out that the above microstructure degradation and oxidation could induce interface failure under long-term low stress conditions (such as actual service conditions in power plants). When the external load was large (such as high-temperature tensile load), the DMW failure would evolve into the ferritic BM failure dominated by plastic deformation.

4 Conclusions

In this study, the failure of DMWs between ferritic heat resistant steels and austenitic stainless steels in practical power plant was analysed by a combination of FEA method and experiments. The effects of mechanics factor, microstructure factor and oxidation factor on failure were comprehensively considered. The main conclusions are as follows.

(1) Under the high-temperature and low-stress service conditions for a long period of service in power plant, the premature failure mode of DMW was along the interface between nickel-based WM and ferritic heat resistant steel. The WM/ferritic steel interface failure of DMW was the result of coupling

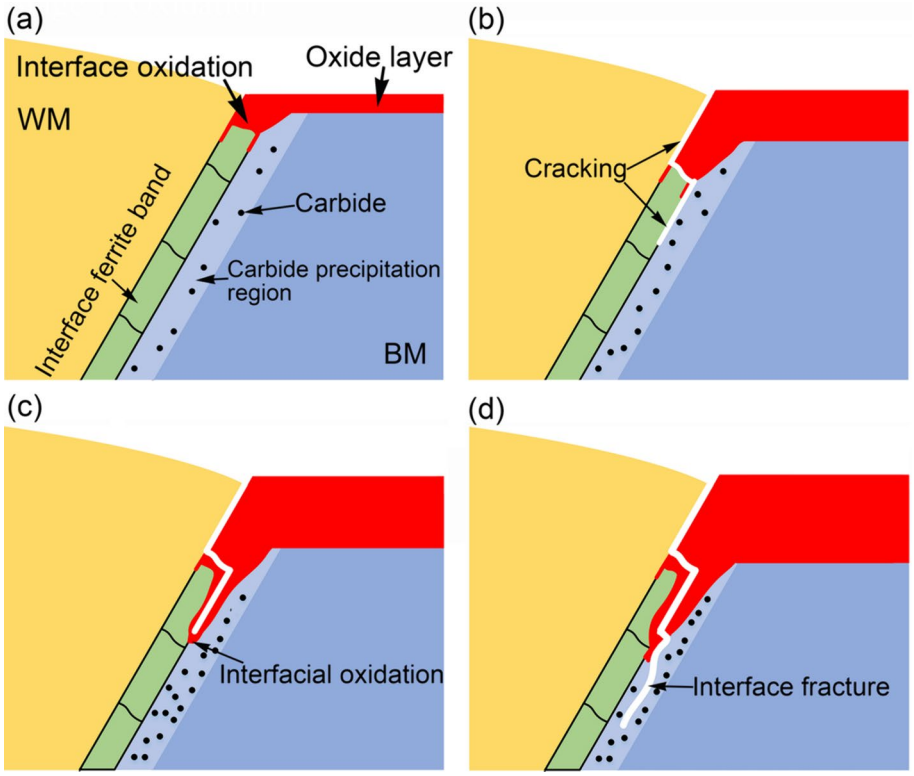

Figure 22 Schematic diagram of development of DMW failure along the interface between the nickel-based WM and ferritic BM

effects of stress/strain concentration, microstructure and oxidation.

(2) The WM/ferritic steel interface stress concentration was induced by thermal stress caused by the difference in CTE and creep strain concentration was related to the creep strength gradient on both sides of the interface. Equivalent creep strain was mainly concentrated at the WM/ferritic steel interface and in its nearby HAZ. Stress and creep strain in DMWs were redistributed during long-term service, and the location where both stress concentration and strain concentration existed was the weak part of the DMWs.

(3) There were both stress and strain concentrations at the WM/ferritic steel interface on the DMW surface, and with the extension of service time the stress and strain concentrations became more and more obvious, which contributed to being an effective driving force for interface failure. Meanwhile, due to obvious creep deformation in the low-alloy steel side, the Mises stress in the DMWs was released.

(4) During long-term service, the ferrite band along the WM/ferritic steel interface was prone to crack triggering by the interface stress concentration, which promoted oxidation along the interface. There was a synergistic effect between interface cracking and interface oxidating, which was the disadvantage that led to the shortened service life of the DMW.

(5) The interface failure of DMW was triggered only under the long-term service of low stress conditions in the practical power plants, not under high-temperature tensile conditions in the laboratory. After long-term service, the *UTS* and the plasticity of DMW were reduced, but the *YS* of it was not significantly affected.

(6) The findings provided guidance for further study aimed at improving service life of DMWs in the practical power plants.

Acknowledgements
Not applicable.

Author Contributions
XL wrote the manuscript; XL and JN were in charge of the whole trial; XW, KL and HZ assisted with result analyses. All authors read and approved the final manuscript.

Funding
Supported by Youth Elite Project of CNNC and Modular HTGR Super-critical Power Generation Technology collaborative project between CNNC and Tsinghua University Project (Grant No. ZHJTIZYFGWD20201).

Data availability
Not applicable.

Declarations

Competing Interests
The authors declare no competing financial interests.

Received: 3 May 2024 Revised: 27 June 2024 Accepted: 1 July 2024
Published online: 23 July 2024

References

[1] F. Abe. Progress in creep-resistant steels for high efficiency coal-fired power plants. *J. Press. Vess-T. ASME*, 2016, 138(4): 040804.
[2] J. N. DuPont. Microstructural evolution and high temperature failure of ferritic to austenitic dissimilar welds. *Int. Mater. Rev.*, 2012, 57(4): 208-234.
[3] J. D. Parker, G.C. Stratford. Review of factors affecting condition assessment of nickel based transition joints. *Sci. Technol. Weld. Joi.*, 1999, 4(1): 29-39.
[4] X. G. Li, K. J. Li, Z. P. Cai, et al. A review of austenite memory effect in HAZ of B con-taining 9% Cr martensitic heat resistant steel. *Metals*, 2019, 9(11): 1233.
[5] J. N. DuPont, S. Babu, S. Liu. Welding of materials for energy applications. *Metall. Mater. Trans. A*, 2013, 44A(7): 3385-3410.
[6] D. I. Roberts, R.H. Ryder, R. Viswanathan. Performance of dissimilar welds in service. *J. Press. Vess-T. ASME*, 1985, 107(3): 247-254.
[7] R. L. Klueh. Dissimilar-metal weld failures in boiler tubing. *Power Engineering*, 1984, 88(2): 52-56.
[8] J. A. Williams, J. D. Parker. Effect of thermal cycling on creep-behavior of 2.25Cr-1Mo/type-316 steel dissimilar metal welds. *Mater. Sci. Technol.*, 1994, 10(10): 915-923.
[9] J. D. Parker, G. C. Stratford. Characterization of microstructures in nickel based transition joints. *J. Mater. Sci.*, 2000, 35(16): 4099-4107.
[10] R. D. Nicholson. Creep-rupture properties of austenitic and nickel-based transition joints. *Met. Technol.*, 1982, 9: 305-311.
[11] K. Laha, K. S. Chandravathi, P. Parameswaran, et al. A comparison of creep rupture strength of ferritic/austenitic dissimilar weld joints of different frades of Cr-Mo ferritic steels. *Metall. Mater. Trans. A*, 2013, 43: 1174-1186.
[12] P. Parameswaran, K. Laha. Role of microstructure on creep rupture behaviour of similar and dissimilar joints of modified 9Cr-1Mo steel. *Procedia Eng.*, 2013, 55: 438-442.
[13] K.-Y. Shin, J.-W. Lee, J.-M. Han, et al. Transition of creep damage region in dissimilar welds between Inconel 740H Ni-based superalloy and P92 ferritic/martensitic steel. *Mater. Char.*, 2018, 139: 144-152.
[14] T. Matsunaga, H. Hongo, M. Tabuchi. Interfacial failure in dissimilar weld joint of high boron 9% chromium steel and nickel-based alloy under high-temperature creep condition. *Mater. Sci. Eng. A*, 2017, 695: 302-308.
[15] J. N. Dupont. Review of dissimilar metal welding for the NGNP helical-coil steam generator. E. United States (Ed.). Office of the Assistant Secretary for Nuclear, Idaho National Laboratory, 2010.
[16] R. L. Klueh, J. F. King. Austenitic stainless steel-ferritic steel weld joint failures. *Weld. J.*, 1982, 61(9): 302s-311s.
[17] L. Xu, Y. Wang, H. Jing, et al. Deformation mechanism and microstructure evolution of T92/S30432 dissimilar welded joint during creep. *J. Mater. Eng. Perform.*, 2016, 25(9): 3960-3971.
[18] J. Cao, Y. Gong, Z.-G. Yang. Microstructural analysis on creep properties of dissimilar materials joints between T92 martensitic and HR3C austenitic steels. *Mater. Sci. Eng. A*, 2011, 528(19-20): 6103-6111.
[19] D. J. Abson, J.S. Rothwell. Review of type IV cracking of weldments in 9–12%Cr creep strength enhanced ferritic steels. *Int. Mater. Rev.*, 2013, 58 (8): 437-473.
[20] L. Falat, M. Svoboda, A. Vyrostkova, et al. Microstructure and creep characteristics of dissimilar T91/TP316H martensitic/austenitic welded joint with Ni-based weld metal. *Mater. Char.*, 2012, 72: 15-23.
[21] J. S. Lee, K. Maruyama. Mechanism of microstructural deterioration preceding type IV failure in weldment of Mod.9Cr-1Mo steel. *Met. Mater. Int.*, 2015, 21(4): 639-645.
[22] M. Tabuchi, H. Hongo, F. Abe. Creep strength of dissimilar welded joints using high B-9Cr steel for advanced USC boiler. *Metall. Mater. Trans. A*, 2014, 45(11): 5068-5075.
[23] Y. Liu, S. Tsukamoto, T. Shirane, et al. Formation mechanism of type IV failure in high Cr ferritic heat-resistant steel-welded joint. *Metall. Mater. Trans. A*, 2013, 44(10): 4626-4633.
[24] K. Laha, K.S. Chandravathi, P. Parameswaran, et al. Characterization of microstructures across the heat-affected zone of the modified 9Cr-1Mo weld joint to understand its role in promoting type IV cracking. *Metall. Mater. Trans. A*, 2007, 38(1): 58-68.
[25] J. A. Francis, W. Mazur, H.K.D.H. Bhadeshia. Review type IV cracking in ferritic power plant steels. *Taylor & Francis*, 2006: 1387-1395.
[26] Y. Zhang, K. J. Li, Z. P. Cai, et al. Creep rupture properties of dissimilar metal weld between Inconel 617B and modified 9%Cr martensitic steel. *Mater. Sci. Eng. A*, 2019, 764: 138185.
[27] M. Yamazaki, T. Watanabe, H. Hongo, et al. Creep rupture properties of welded joints of heat resistant steels. *CSEE J. Power Energy*, 2008, 2(4): 1140-1149.
[28] J. Akram, P. R. Kalvala, M Misra, et al. Creep behavior of dissimilar metal weld joints between P91 and AISI 304. *Mater. Sci. Eng. A*, 2017, 688: 396-406.
[29] X. G. Li, J. F. Nie, X. Wang, et al. Evolution mechanism of interfacial microstructure and its effect on failure in dissimilar metal welds containing ferritic heat resistant steels. *J. Mater. Sci. Technol.*, 2023, 26: 6565-6580.
[30] X. G. Li, Z. P. Cai, X. Chen, et al. Characterization and formation mechanism of ultra-fine ferrite grains in dissimilar metal weld between austenitic stainless steel and low alloy ferritic steel. *Mater. Charact.*, 2021, 171: 110777.
[31] J. D. Parker, G. C. Stratford. The high-temperature performance of nickel-based transition joints: II. Fracture behavior. *Mater. Sci. Eng. A*, 2001, 299: 174-184.
[32] X. G. Li, Z. P. Cai, X. Chen, et al. Oxidation damage and interfacial failure of dissimilar metal welds containing ferritic heat resistant steels. *J. Iron Steel Res. Int.*, 2021, 28: 1439-1450.
[33] D.R.H. Jones. Creep failures of overheated boiler, superheater and reformer tubes. *Eng. Fail. Ana.*, 2004, 11(6): 873-893.
[34] J. Q. Zhang, Y. Tang, G. D. Zhang, et al. Numerical simulation on interfacial creep failure of dissimilar metal welded joint between HR3C and T91 heat-resistant steel. *Journal of Wuhan University of Technology*, 2016, 31(5): 1068-1074.
[35] Y. M. Li, C. X. Fan, B. X. Yang, et al. New heat-resistant steel for large thermal power units. *China Electric Power Press*, 2013. (in Chinese)
[36] J. F. Wen, S. T. Tu, X. L. Gao, et al. New model for creep damage analysis and its application to creep crack growth simulations. *Mater. Sci. Tech-Lond*, 2014, 30(1): 32-37.
[37] S. Goyal, K. Laha, C. R. Das, et al. Finite element analysis of effect of triaxial state of stress on creep cavitation and rupture behaviour of 2.25Cr–1Mo steel. *Int. J. Mec. Sci.*, 2013, 563(15): 68-77.
[38] S. Goyal, K. Laha, C. R. Das, et al. Analysis of creep rupture behavior of Cr-Mo ferritic steels in the presence of notch. *Metall Mater Trans A*, 2015, 46: 205-217.
[39] X. Du, D. Liu, Y. Liu. Numerical limit load analysis of 3D pressure vessel with volume defect considering creep damage behavior. *Math. Probl. Eng.*, 2015, 2015:1-13.
[40] M. Tabuchi, H. Hongo, Y. Li, et al. Evaluation of microstructures and creep damages in the HAZ of P91 steel weldment. *J Pres Vessel Technol*, 2009, 131(2): 21406.
[41] X. G. Li, J. F. Nie, X. Wang, et al. Effect of interface form on creep failure and life of dissimilar metal welds involving nickel-based weld metal and ferritic base metal. *Chin. J. Mech. Eng.*, 2024, 37: 18.
[42] Y. Zhang, M. J. Hu, Z. P. Cai, et al. Effect of nickel-based filler metal types on creep properties of dissimilar metal welds between Inconel 617B and 10% Cr martensitic steel. *J. Mater. Sci. Technol.*, 2021, 14: 2289-2301.
[43] M. Kamaya, A. J. Wilkinson, J. M. Titchmarsh. Quantification of plastic strain of stainless steel and nickel alloy by electron backscatter diffraction. *Acta Mater.*, 2006, 54(2): 539-548.
[44] D. Kobayashi, M. Miyabe, Y. Kagiya, et al. An assessment and estimation of the damage progression behavior of IN738LC under various applied stress conditions based on EBSD analysis. *Metall. Mater. Trans. A*, 2013, 44(7): 3123-3135.

[45] S. S. Rui, Y. B. Shang, Y. N. Fan, et al. EBSD analysis of creep deformation induced grain lattice distortion: A new method for creep damage evaluation of austenitic stainless steels. *Mater. Sci. Eng. A*, 2018, 733: 329-337.
[46] X. G. Li, J. F. Nie, X. Wang, et al. Microstructure evolution at Ni/Fe interface in dissimilar metal weld between ferritic steel and austenitic stainless steel. *Materials*, 2023, 16, 6294.
[47] K. J. Li, X. G. Li, Y. Zhang, et al. Microstructure evolution and high temperature failure mechanism of dissimilar metal welded joints. *Electric Welding Machine*, 2020, 50(09): 17-43.
[48] S. Orzolek, J. DuPont, J. Siefert. Microstructural evolution of dissimilar metal welds involving Grade 91. *Metall Mater Trans A*, 2020(51): 2222-2238.

Xiaogang Li born in 1992, is currently an Assistant Professor at *Institute of Nuclear and New Energy Technology, Tsinghua University, China*. He received his PhD degree from *Tsinghua University, China*, in 2022.

Junfeng Nie born in 1982, is currently an associate Professor at *Institute of Nuclear and New Energy Technology, Tsinghua University, China*. He received his PhD degree from *Tsinghua University, China*, in 2009.

Xin Wang born in 1979, is currently a Research Engineer at *Institute of Nuclear and New Energy Technology, Tsinghua University, China*. He received his Master degree from *Tsinghua University, China*, in 2009.

Kejian Li born in 1989, is currently an associate Professor at *Department of Mechanical Engineering, Tsinghua University, China*. He received his PhD degree from *Tsinghua University, China*, in 2016.

Haiquan Zhang born in 1970, is currently a Professor at *Institute of Nuclear and New Energy Technology, Tsinghua University, China*. He received his PhD degree from *Beihang University, China*, in 2002.